Experiments in Fluids 30 (2001) 65–72 © Springer-Verlag 2001

Simultaneous DPTV/PLIF measurements of a turbulent jet

D. R. Webster, P. J. W. Roberts, L. Ra'ad

Abstract Simultaneous measurements of instantaneous velocity and concentration fields were performed using digital particle tracking velocimetry and planar laser-induced fluorescence for a turbulent jet at a Reynolds number of 3000. The measurements of mean velocity, turbulent stresses, mean concentration, concentration variance, and turbulent flux of tracer all collapse onto self-similar profiles in the far field of the jet. The measurements showed excellent agreement with previous point velocity and concentration measurements. It is concluded that the system is an effective means of measuring the velocity and concentration distributions and turbulent characteristics.

1 Introduction

Transport of a scalar quantity, such as chemical concentration or temperature, is important in many engineering applications and environmental flows. Measurements of the turbulent transport are useful for the design of many devices, including mixers, chemical reactors, and combustion chambers. In addition, understanding the turbulent transport is very important in environmental flows where mixing and dilution of chemicals and pollutants affect safety and quality of life.

The purpose of this study was to develop a high-resolution simultaneous velocity and concentration field measurement technique for turbulent flows. Field measurement techniques such as digital particle image velocimetry (DPIV) and planar laser-induced fluorescence (PLIF) measure the instantaneous spatial distribution of velocity and concentration, respectively. These are non-intrusive techniques that are superior to point measurements because they reveal the instantaneous spatial relationships that are important for understanding complex turbulent flows.

Received: 7 July 1999/Accepted: 9 February 2000

D. R. Webster (✉), P. J. W. Roberts, L. Ra'ad
School of Civil & Environmental Engineering,
Georgia Institute of Technology,
Atlanta, GA 30332-0355, USA

The authors gratefully acknowledge the financial support of DARPA/ONR. Special thanks to Professor Todd Cowen for providing access to the DPTV processing algorithm.

Simultaneous measurements of the velocity field via digital particle tracking velocimetry (DPTV) and the concentration field via PLIF are performed. DPTV is part of a broad class of techniques that measure the fluid velocity by observing the displacement of tracer particles over a short time delay. The tracers are located by recording brief pulses of laser light scattered from the particles on a medium such as film or a video array detector. Consecutive images are compared to determine the local particle displacement. Combining the displacement estimates with the image magnification and time delay between laser pulses yields the velocity field. While DPIV utilizes the cross-correlation between images to determine the average displacement in a particular sub-window, DPTV tracks individual particles. The DPTV analysis method is more computationally intensive and produces a non-uniform grid of vectors. The vector density is significantly higher, however, with improved spatial resolution, accuracy, and ultimately turbulent statistics (Cowen and Monismith 1997).

Measuring the concentration field with the PLIF technique involves exciting a fluorescent dye tracer with light at a wavelength within its absorption range. The dye emits longer-wavelength light with intensity proportional to the local dye concentration and laser light intensity. After careful calibration, the digital images of the instantaneous intensity distribution are converted to the concentration field.

This paper includes data collected for a turbulent round jet at a Reynolds number of 3000. Turbulent round jets have received significant attention in the literature, including Wygnanski and Fiedler (1969), Antonia et al. (1975), Papanicolaou and List (1988), and many others. To validate the technique, the measurements are compared with the point velocity and concentration measurements available in these papers.

Of particular interest to this study are the radial and axial turbulent flux of a passive tracer. The measurements afford us the opportunity to calculate the local covariance between concentration and velocity fluctuations, $\overline{u'c'}$ and $\overline{v'c'}$. To calculate these quantities, the vectors resulting from the DPTV analysis are correlated with the simultaneous concentration measurement at the same pixel location. Since the instantaneous and mean concentration values have been calculated at each point in the field, it is a relatively straightforward procedure to calculate the covariance at each location where a validated vector was identified.

2
Experimental apparatus

The experiments were performed in a 1.07-m-wide by 24.4-m-long tilting flume with a rectangular cross section. The flume was dammed at the tail end to provide a stationary ambient volume while the jet measurements were performed.

As shown in Fig. 1, laser sheet access was provided by the glass sidewalls of the flume. The cameras were mounted above the test section. To eliminate the optical distortion of photographing through the free surface, a 19-mm-thick acrylic sheet was supported at the water surface such that the bottom surface was wetted.

The jet discharged from a brass 3.14-mm-inner diameter round nozzle. The straight brass tube was sufficiently long to create fully developed turbulent pipe flow conditions at the discharge nozzle. The source discharge system delivered the effluent from a 40-l polyethylene tank. A rotameter measured the flow rate controlled by a needle valve.

The illumination pulses were generated with two Nd: YAG lasers (Gemini model, New Wave Research Inc.). After passing through a second harmonic generator, the emitted wavelength was 532 nm. The energy level for each laser was 130 mJ per pulse, and the pulse duration was 6 ns. The laser beam paths were combined with a polarized mirror inside the combined laser head housing. The laser beam diameter was approximately 4.5 mm. A combination of lenses focused and expanded the beam into a thin sheet. The lenses were 1000 mm focal length spherical and –12.7 mm focal length cylindrical plano-concave. The spherical lens focused the sheet to approximately 1.0 mm thick in the photographic region, while the cylindrical lens expanded the sheet to span the entire photographic region.

Two Kodak MegaPlus ES 1.0 CCD cameras captured the DPTV and PLIF images. The cameras produced 8-bit digital images with 1008 horizontal and 1018 vertical pixels. The ES 1.0 features an electronic shutter and a unique double-frame mode. The timing sequence was such that the first frame of each camera was exposed by the first laser firing and then transferred from the light-sensitive cells to the storage cells. While the first image was transferred to the frame grabbing board, the second image was exposed to the illumination of the second laser. The time delay between the laser pulses was 10.0 ms.

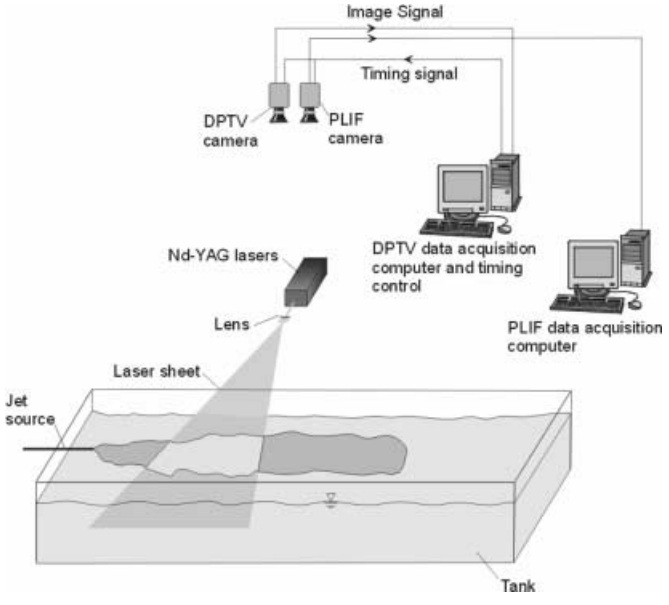

Fig. 1. Schematic of apparatus

The cameras were mounted side by side on a support carriage. Precision tilt and rotation stages adjusted the camera orientation so that they photographed the same region of the laser sheet. After photographing a ruled grid, the collected images were shifted (less than 10 pixels in each direction) to produce perfectly aligned images.

Both cameras used identical 60-mm Nikon aberration-free lenses. Two filters were placed on each camera, a clear filter to block the UV wavelengths and a standard hot mirror filter to block the IR wavelengths. Blocking the IR light is important because the fundamental Nd: YAG wavelength is 1064 nm and may damage the CCD chip.

A laser-line optical filter (Omega Optical Inc.) on the DPTV camera allowed only the scattered laser light to pass. The filter passed 87% of the light at 532 nm and had a bandwidth of 3 nm. This filter therefore effectively blocked the yellow/orange light emitted by the Rhodamine dye (used by the PLIF technique) while passing the green light scattered by the suspended particles. Thus, images were captured with sufficient contrast between the suspended particles and background for the particle identification procedure.

An optical high pass filter (Tiffen 21) with cutoff around 560 nm was placed on the PLIF camera. The filter effectively blocked the 532-nm laser light scattered from the seeding particles used by the DPTV technique. It was very important to block the scattered green light because it would appear as false high concentration pixels in the processed concentration fields.

Video Savant RTD software for Windows NT was used to capture, process, and store images from each digital camera. Images were stored directly on the hard drive array in real time, a process referred to as real-time-to-disk (RTD). For this experiment, several minutes of digital video were required to achieve statistically stationary data and to provide a lengthy, continuous record of velocity and concentration.

3
Experimental procedure

The experiments were performed in water at 20 °C. The jet velocity at the nozzle, U_0, was 0.95 m/s corresponding to a Reynolds number of 3000.

We have chosen Rhodamine 6G as the fluorescent dye because the peak absorption is at 530 nm, very close to the wavelength of Nd: YAG laser light. The peak emission of Rhodamine 6G is near 560 nm (Arcoumanis et al. 1990). Thus, the green laser light and yellow/orange emission light could be effectively isolated with the optical filters described above.

Previous researchers have observed that residual chlorine reacted with Rhodamine 6G, causing decay in concentration (Davidson et al. 1997). Sodium thiosulfate

was added to both the ambient and the effluent water to remove any residual chlorine, and a commercial chlorine test kit was used to verify the removal. A premixed high concentrate Rhodamine 6G dye solution was added to the effluent water to produce a dye solution of 200 μg/l.

Titanium dioxide (TiO_2) particles with a specific gravity of 3.5 and nominal diameter less than 5 μm were used as tracers. A small amount of TiO_2 (<0.5 g) was added to both the ambient and effluent fluid. The metal oxide particles provide superior light scatter to comparably sized nylon or kaolin particles. The inertial time constant of the particles was approximately 2 μs, and the settling velocity was 12 μm/s, both of which are negligibly small for this flow.

The PLIF technique required a careful calibration to convert image intensity to concentration. The calibration procedure was performed in the flume with identical optical conditions to the jet experiments, except that the dam at the tail end was removed. A copper, 38.1-mm-diameter diffuser with eight 1.6-mm-diameter holes spanned the flume at mid-depth near the head box. A 1.0-g/l solution of Rhodamine 6G was pumped to the diffuser at controlled flow rates to create calibration concentration levels. The dye was ejected from the diffuser as high velocity jets and mixed further due to ambient turbulence while advecting down the flume, creating a uniform concentration distribution at the measurement region. Eighty images were captured for each of six concentration levels, between 0 and 25 μg/l. (Concentration levels were maintained at this low level to minimize absorption effects.) The 80 images were averaged to produce a single calibration image for a given concentration level. The averaging removed any slight non-uniformity of dye concentration. The calibration images were correct for attenuation of laser intensity using the coefficients reported in Ferrier et al. (1993). The pixel response was found to be closely linear and a calibration curve was applied to each pixel.

4
Image processing

In this experiment, the double frame capture rate was 10 Hz and 4000 consecutive images were captured simultaneously by each camera. The total duration of the sampling was thus 200 s, which was significantly longer than the largest time scales in the jet flow. The 4 GB RTD file was subsequently converted by Video Savant to individual 1 MB TIFF image files for processing. One thousand fields were found to be sufficient to achieve statistically stationary turbulence data; thus every other image pair was used in the statistical calculations.

The DPTV technique employed here follows the method of Cowen and Monismith (1997). The DPTV processing employed the following steps: preconditioning of the images, coarse DPIV analysis, DPIV validation, DPTV algorithm, and DPTV validation and statistics calculation.

Preconditioning of the images consisted of subtracting the minimum value at each pixel from all the original images. This process removed any constant background level and any effects of non-uniform illumination.

A coarse DPIV vector field was calculated and subsequently used as a displacement estimator for the DPTV search algorithm. In the DPIV algorithm, spatial correlations between two sequential digital images were calculated for 64 × 64 non-overlapping subwindows. The correlation was efficiently calculated by complex conjugate multiplication of the spatial Fourier transform of each subwindow. The position of the peak in the correlation corresponded to the average particle displacement within the interrogation subwindow. The correlation peak location was identified to sub-pixel accuracy using a Gaussian-fit function. The second image subwindow was then shifted to be centered at the initial displacement estimate and the correlation calculation was repeated. This procedure was repeated until the displacement vector remained centered in the second image subwindow.

A Gaussian filter was used to remove the occasional stray or bad vector from the DPIV algorithm. To accomplish this, the mean and standard deviation were calculated at each location using all 1000 vector fields. Vectors falling beyond ±4 standard deviations were discarded. The filter was repetitively applied until no additional vectors were removed.

The filtered DPIV velocity field was then used to develop a displacement estimating function for the velocity at any point in the field.

The DPTV algorithm consists of the following steps. Both images in the pair were binarized with a threshold value of 50 between a pixel and the background. The binary image was then scanned to identify clusters of light pixels, which denote particles. The center of each particle was determined to sub-pixel accuracy by a Gaussian-fit function to the original image.

When particle pairs are matched, the displacement of each particle identified in the first image is first estimated using the estimating function discussed above. A local correlation over 9 × 9 subwindows was performed to refine the displacement estimate. Finally, a 3 × 3 subwindow centered at the refined displacement estimate location was examined. If one, and only one, particle was present in that window, the particles were considered a pair. The displacement vector was then calculated as the difference between the particle locations.

The result of the DPTV algorithm was randomly placed vectors of considerably higher density than the uniform DPIV field. The fields were divided into 32 × 32 subwindows to calculate the flow statistics. Any vector falling in a particular subwindow for any of the 1000 vector fields was included in the statistics. Stray vectors are removed with the dynamic Gaussian filter described above. For this data set, approximately 4000 validated vectors were used in each subwindow.

PLIF image pairs were captured at the same instants as the DPTV image pairs. The PLIF image pairs were then averaged to yield an image that corresponded to the mid-time between the laser pair firings, in agreement with the velocity estimate. The PLIF processing used the fact that the intensity of light emitted from the fluorescent dye is proportional to the concentration and incident light intensity.

The calibration procedure accounted for laser sheet non-uniformity, pixel response non-uniformity, and lens vignette. Each pixel in the field was calibrated separately.

A linear regression was applied to the six calibration images of known concentrations to yield a slope and intercept at 1008 × 1018 pixel locations. The raw image files were then converted to concentration levels by applying the linear calibration function to each pixel. Statistical quantities such as the mean and variance were then calculated at each pixel location.

Once the velocity and concentration fields are calculated, it is relatively straightforward to calculate the covariance between the velocity and concentration:

$$\overline{u'c'} = \frac{1}{N}\sum_{1}^{N}(u-U)(c-C)$$

where the upper-case symbols are mean quantities and the lower-case symbols are instantaneous quantities. Individual validated velocity vectors resulting from the DPTV analysis were correlated with the concentration value located at the center of the vector. The correlation values were then averaged over 32 × 32 subwindows in the same manner as the velocity statistics.

The measurement uncertainty for velocity was estimated to be ±2% based on the accuracy of the particle location estimate. The uncertainty in the concentration measurement was estimated to be ±3% based on several factors including the calibration procedure and repeatability of the laser sheet intensity.

5 Results

A sample velocity field obtained by processing a DPTV image pair is shown in Fig. 2a. Figure 2b shows the simultaneous concentration field, where the contour levels represent Rhodamine 6G concentration levels nondimensionalized by C_0, the source concentration. The coordinate axes have been non-dimensionalized by the nozzle diameter, D. As expected, the jet width increases with downstream distance, while the concentration and velocity magnitudes decrease. The decay of mean centerline velocity, shown in Fig. 3, agrees very well with the semi-empirical curve reported by Fischer et al. (1979), $U_c = 6.2\, DU_0/x$, where U_c is the mean centerline velocity. The growth and dilution of the jet result from entrainment of low-concentration, low-momentum fluid from the ambient into the jet. Entrainment and ejection events can be observed in the velocity field. In addition, the concentration contours show the jet interface to be highly contorted due to the presence of a range of turbulent eddy sizes.

At large downstream distances, previous experiments show that the flow becomes self-preserving, which means that the local length and velocity scales solely determine both the mean and the turbulent fields. To observe self-similar behavior, profiles were examined in the zone of established flow (ZEF), which exists beyond approximately 6D downstream from the jet nozzle (Fischer et al. 1979). Eight mean velocity profiles are shown in Fig. 4. The local velocity scale is represented by U_c. Because the jet width grows linearly, the local length scale is proportional to downstream distance (Tennekes and Lumley 1972). The eight profiles collapsed onto a single profile, thus confirming that the flow was self-similar. Also shown in Fig. 4 is the semi-empirical curve given by Fischer et al. (1979), $U = U_c \exp\{-(r/b_u)^2\}$, where r is the radial distance from the jet axis, $b_u = 0.107x$ is a measure of the half-width of the mean velocity profile, and x is the downstream distance from the nozzle. The coefficient 0.107 is the average of several experimental investigations of round jets (Fischer et al. 1979). The present data agree remarkably well with this expression.

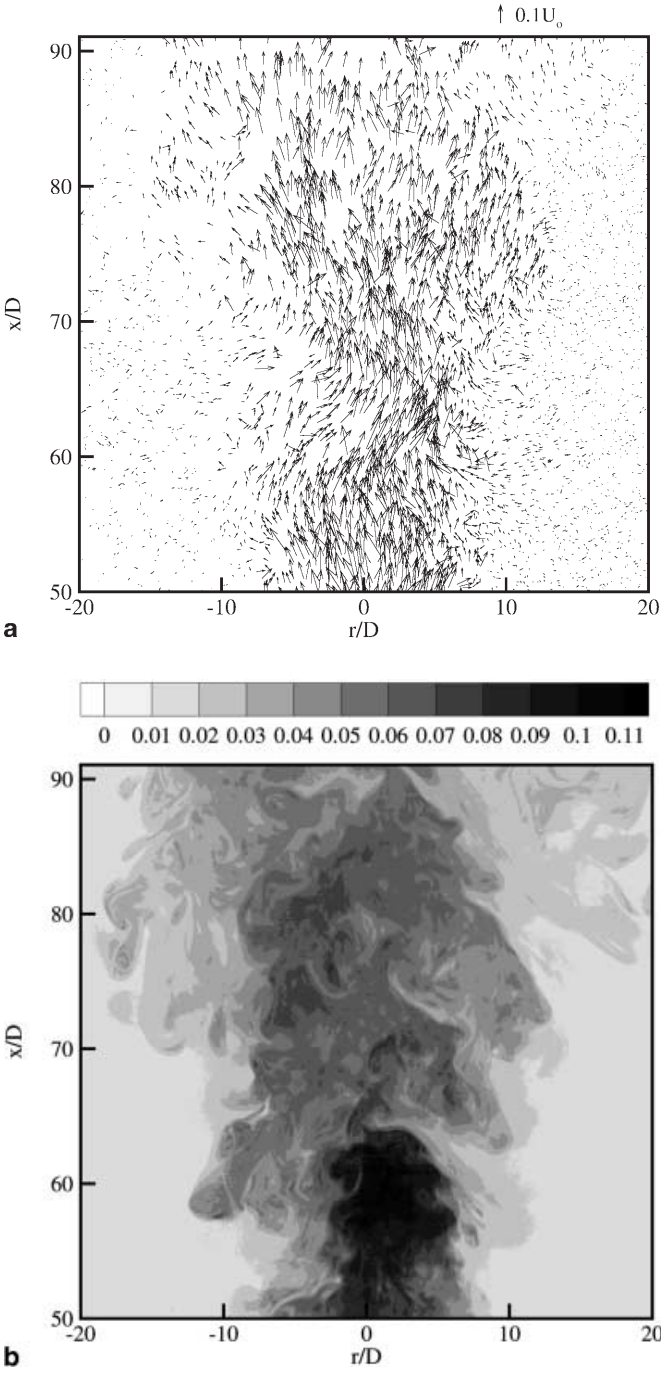

Fig. 2. **a** Sample simultaneous velocity field. **b** Sample simultaneous concentration field

Figures 5–7 show eight profiles of axial normal stress, $\overline{u'u'}$, radial normal stress, $\overline{v'v'}$, and shear stress, $\overline{u'v'}$. Again, the local velocity scale is the mean centerline velocity and

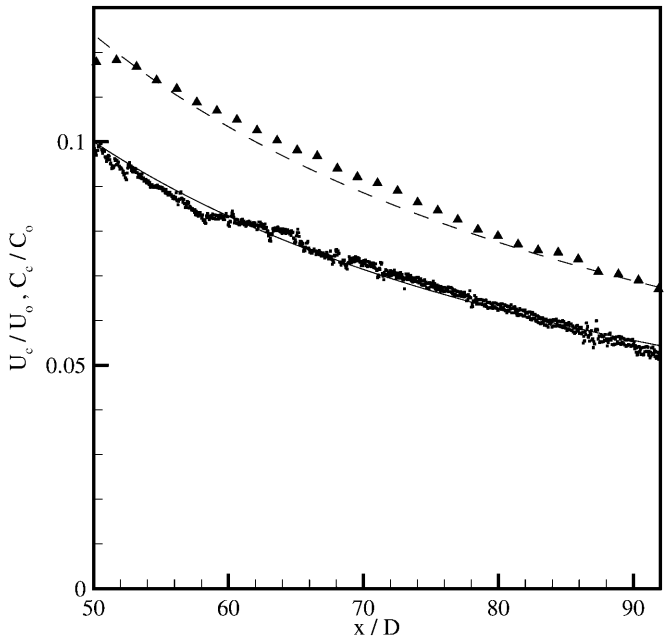

Fig. 3. Mean velocity (*triangle*) and tracer concentration (*square*)along the jet centerline. Also shown are the semi-empirical curves $U_c = 6.2\ DU_0/x$ (*dashed line*) and $C_c = 5\ DC_0/x$ (*solid line*) reported by Fischer et al. (1979)

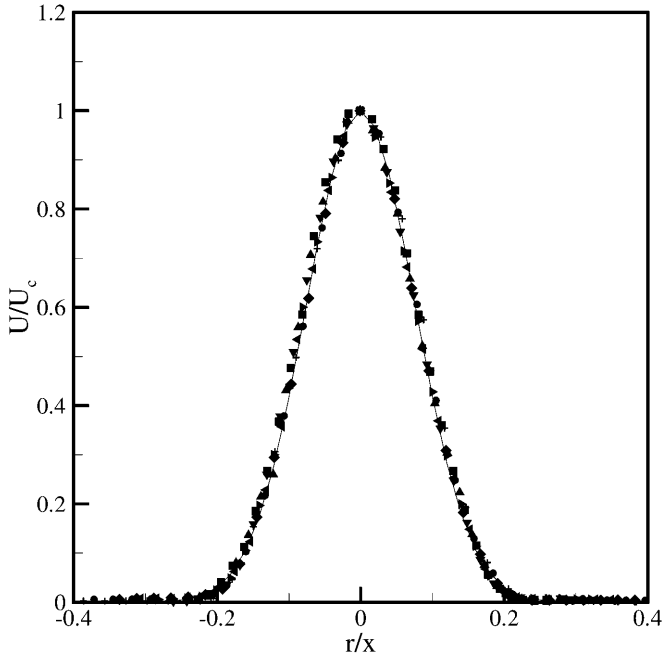

Fig. 4. Self-similar mean velocity profiles. Symbols correspond to $x/D = 50$ (*cross*), 56 (*circle*), 62 (*diamond*), 68 (*arrowhead pointing left*), 74 (*arrowhead pointing right*), 80 (*arrowhead pointing down*), 86 (*arrowhead pointing up*) and 92 (*square*)

the local length scale is characterized by downstream distance. In each case, the profiles are self-similar, with slight scatter near the centerline for the normal stresses and near the peak values for the shear stress. The axial and radial normal stresses are positive and symmetric about the centerline, as expected. The shear stress is antisymmetric about the centerline: positive where the mean shear is negative and negative where the mean shear is positive. The sign of the shear stress agrees with the net transport of high momentum away from the centerline.

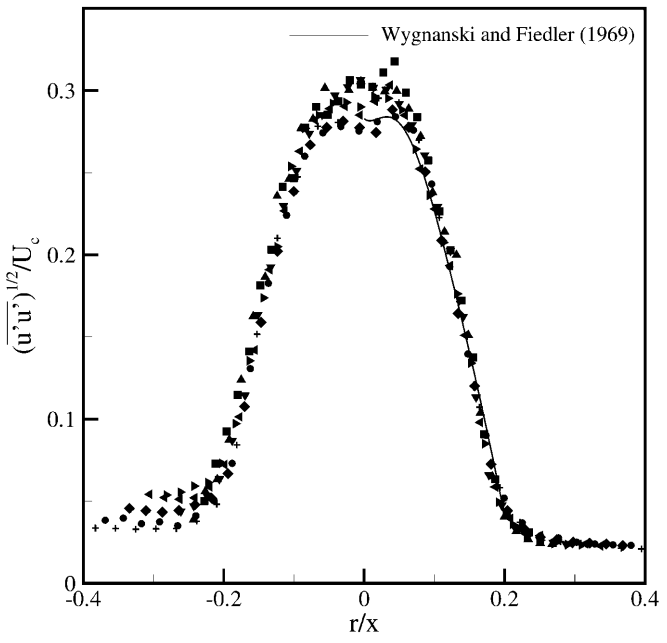

Fig. 5. Self-similar axial normal stress profiles. Symbols same as Fig. 4

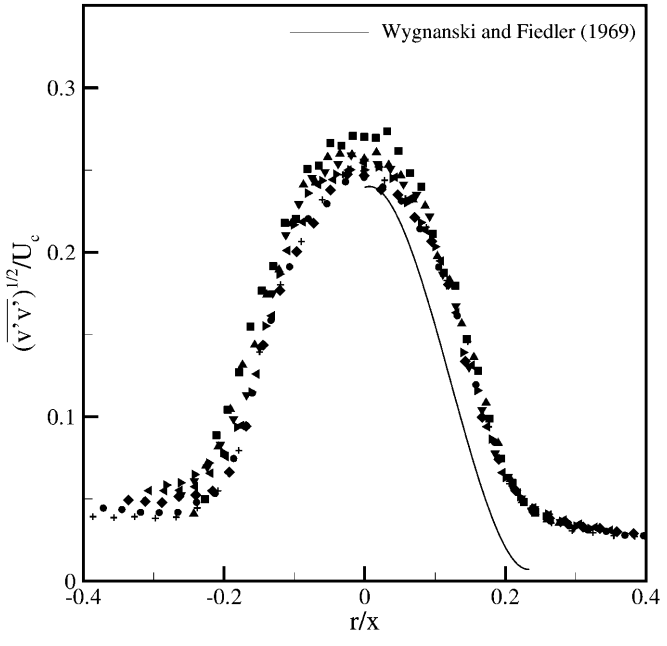

Fig. 6. Self-similar radial normal stress profiles. Symbols same as Fig. 4

The current measurements of axial normal stress agree very well with those of Wygnanski and Fiedler (1969), which were performed with hot-wire anemometry. While the agreement with Wygnanski and Fiedler (1969) is remarkable, it should be noted that reported centerline values in the literature vary between 0.24 and 0.3

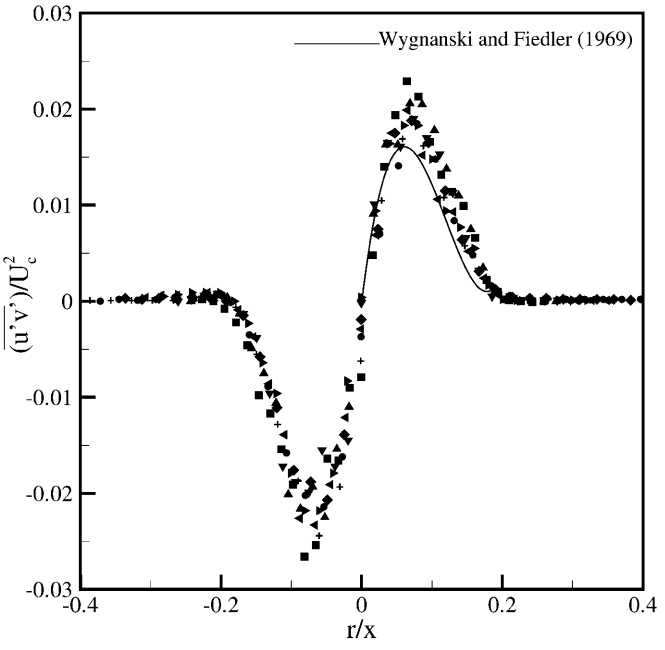

Fig. 7. Self-similar shear stress profiles. Symbols same as Fig. 4

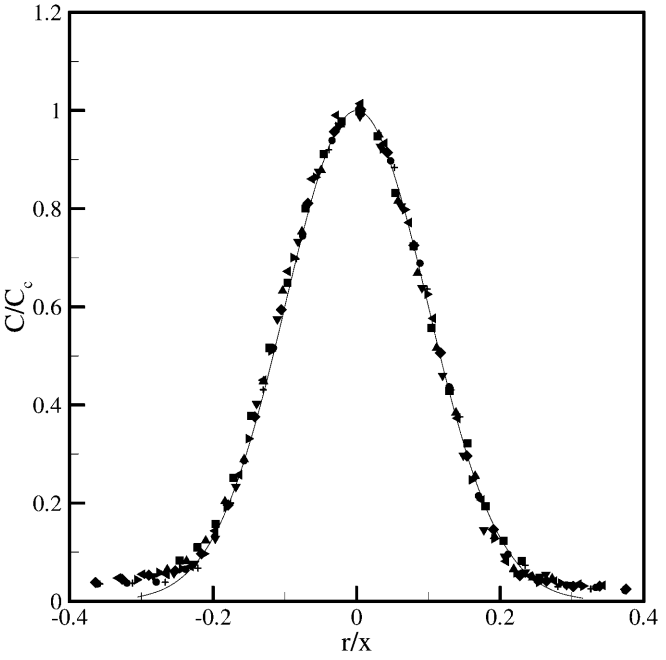

Fig. 8. Self-similar mean concentration profiles. Symbols same as Fig. 4

(e.g., Gibson 1963; Antonia et al. 1975; Chevray and Tutu 1978; Papanicolaou and List 1988).

The measured values of radial normal stress are slightly higher than those reported by Wygnanski and Fiedler (1969), while the profile shape seems to agree well. There is more disparity among the reported measurements of this quantity in the literature than in the axial component; centerline values have been reported between 0.18 and 0.3. The present results fall roughly in the middle of this range.

The shear stress measurements compare well with the profile of Wygnanski and Fiedler (1969), although the peak value is slightly higher in the present measurements. Again, some disparity is observed in previous measurement of the peak value of this quantity with the present measurements falling roughly in the middle of the range. The location of the peak is consistent with Wygnanski and Fiedler (1969) and corresponds to the location were the mean velocity gradient is greatest.

Concentration measurements also agree well with previous studies. The mean concentration decay along the centerline, shown in Fig. 3, agrees well with the semi-empirical curve reported by Fischer et al. (1979), $C_c = 5\ DC_0/x$. Figure 8 shows the self-similar mean concentration profiles. The characteristic concentration is the mean centerline value, C_c, and the length scale is characterized by x, as with the velocity profiles. The mean concentration field is symmetric about the centerline, as expected.

Also shown in Fig. 8 is the semi-empirical curve by Fischer et al. (1979), $C = C_c \exp\{-(r/b_c)^2\}$, where the half-width of the concentration field is $b_c = 0.140x$. The coefficient 0.140 is slightly higher than the average (0.127) of several experimental data sets reported by Fischer et al. (1979), but falls within the range of quoted values ($0.101 < b_c < 0.156$). With this choice of coefficient, the present data agree very well with the Gaussian curve. The ratio b_c/b_u is 1.30, indicating the concentration field spreads roughly 30% faster than the velocity field. The increased growth rate indicates the turbulent transport of the scalar is larger than that of momentum.

Figure 9 shows eight profiles of the concentration standard deviation, $(\overline{c'c'})^{1/2}$, normalized by the centerline mean value, C_c. The profiles are symmetric about the centerline, and the peak value is displaced off the centerline. The profiles collapse onto a self-similar shape, and agree well with the measurements of Papanicolaou and List

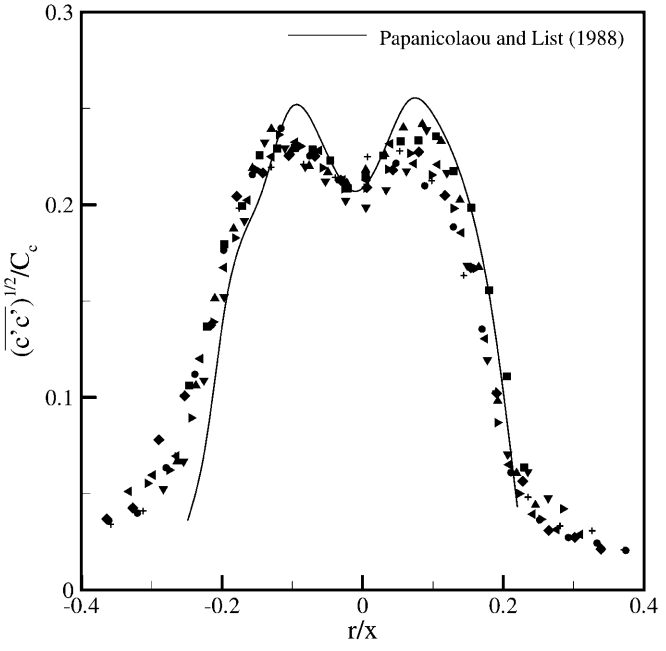

Fig. 9. Self-similar concentration variance profiles. Symbols same as Fig. 4

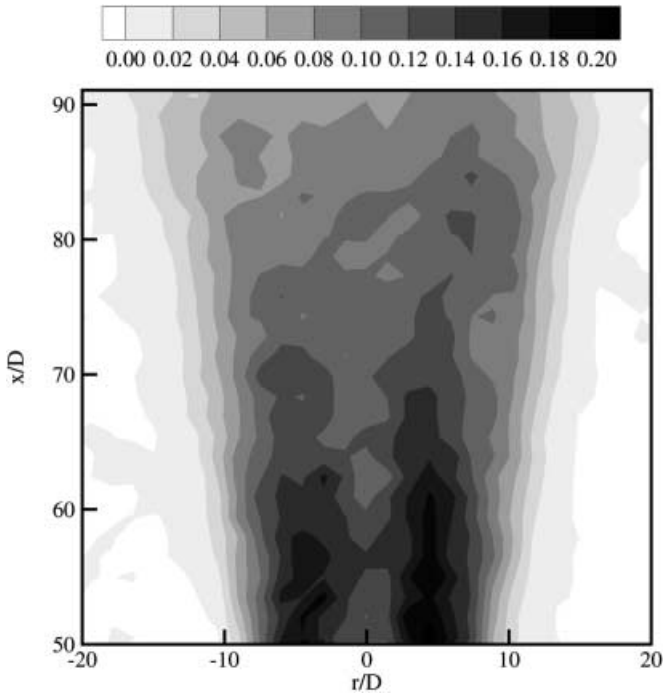

Fig. 10. Contours of the axial turbulent flux, 1000 $\overline{u'c'}/U_0C_0$

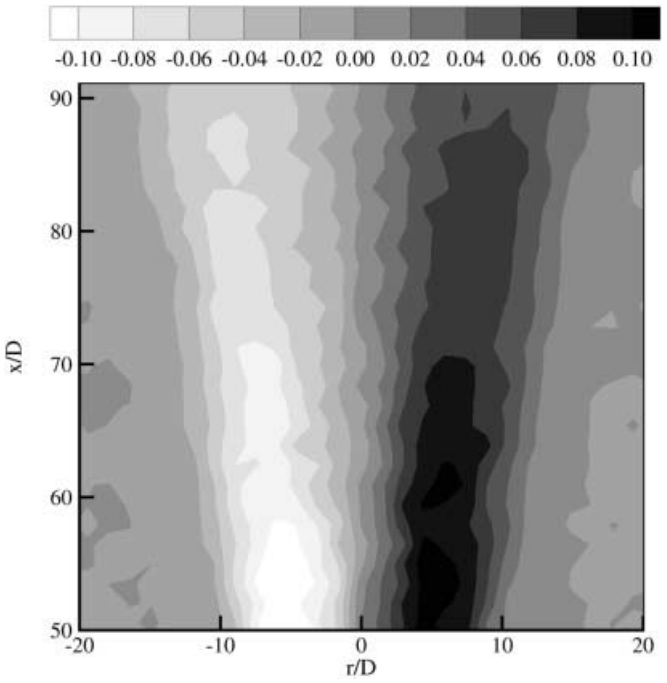

Fig. 11. Contours of the radial turbulent flux, $\overline{v'c'}/U_0C_0$

(1988), who used a combined laser Doppler velocimetry (LDV) and laser-induced fluorescence (LIF) system to measure simultaneous velocity and concentration at single points. The off-centerline location of the maximum occurs at approximately $r/x = 0.1$. The peak location is coincident with the maximum turbulent shear stress observed in Fig. 7.

Figures 10 and 11 show contour plots of the axial turbulent flux, $\overline{u'c'}$, and radial turbulent flux, $\overline{v'c'}$, respectively. In each case, the nozzle exit velocity and concentration are used to non-dimensionalize the flux quantities. The axial turbulent flux is symmetric about the centerline, and the peak value is located off the centerline of the jet, as with the concentration variance. Conversely, the plot of radial turbulent flux is antisymmetric about the centerline. The sign of the radial turbulent flux indicates that the direction of the turbulent flux transport is away from the centerline.

Self-similar profiles of the axial turbulent flux, $\overline{u'c'}$, are shown in Fig. 12. The turbulent flux is non-dimensionalized by the mean centerline velocity and concentration, so this quantity corresponds to the ratio of turbulent flux to the mean advective flux. Although the data collapses away from the centerline, significant scatter is observed near the centerline. Similar levels of scatter are observed in the data of Papanicolaou and List (1988) (LDV/LIF), Lemoine et al. (1996) (LDV/LIF), and Law and Wang (1998) (PIV/PLIF). Despite the scatter, the present measurements are in reasonable agreement with the referenced studies.

Self-similar profiles of the radial turbulent flux, $\overline{v'c'}$, are shown in Fig. 13. The profiles collapse very well and exhibit less scatter than observed with the axial turbulent flux profiles. The profiles also show excellent agreement with the measurements of Law and Wang (1998).

6 Conclusions

A technique has been developed and tested to measure the planar velocity and concentration distribution in turbulent flows simultaneously with DPTV and PLIF. A simple round jet into a stationary medium was studied to benchmark the measurement system against previous point measurements. Normalized plots of mean velocity, turbulent stresses, mean concentration, and concentration

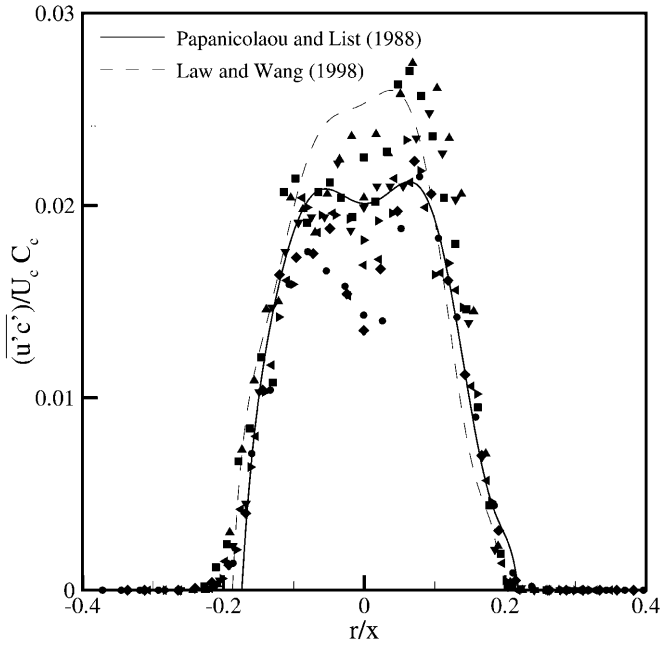

Fig. 12. Self-similar axial turbulent flux profiles. Symbols same as Fig. 4

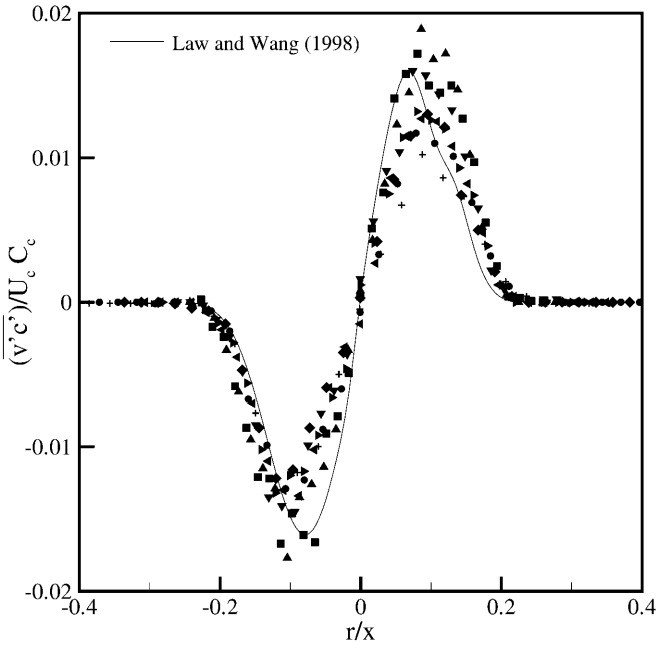

Fig. 13. Self-similar radial turbulent flux profiles. Symbols same as Fig. 4

variance all collapsed to self-similar curves. In each case, the profile shape and magnitude agreed well with previous point velocity and concentration measurements. Normalized profiles of the covariance between velocity and concentration also demonstrated self-similar behavior and agreed well with previous results. As a result of these comparisons, it was concluded that the combined DPTV and PLIF measurement system is an effective and efficient experimental method.

The intention is to use the measurement system to study complex environmental flows. Understanding the chemical and pollutant transport in many environmental flows is critically important for engineering design, safety, and quality of life considerations. The measurement system described here provides the means to measure the turbulent flux of chemical tracers in such flows.

References

Antonia RA; Prabhu A; Stephenson SE (1975) Conditionally sampled measurements in a heated turbulent jet. J Fluid Mech 72: 455–480

Arcoumanis C; McGuirk JJ; Palma JMLM (1990) On the use of fluorescent dyes for concentration measurements in water flows. Exp Fluids 10: 177–180

Chevray R; Tutu NK (1978) Intermittency and preferential transport of heat in a round jet. J Fluid Mech 88: 133–160

Cowen EA; Monismith SG (1997) A hybrid digital particle tracking velocimetry technique. Exp Fluids 22: 199–211

Davidson MJ; Pun KL; Wang HJ (1997) Applications of laser induced fluorescence and image processing in observing plume behavior. Proc 3rd Int Conf on Fluid Dyn Measurement and its Applications, International Academic, Beijing, China, pp 144–149

Ferrier AJ; Funk DR; Roberts PJW (1993) Application of optical techniques to the study of plumes in stratified fluids. Dyn Atmos Oceans 20: 155–183

Fischer HB; List EJ; Koh RCY; Imberger J; Brooks NH (1979) Mixing in inland and coastal waters. Academic Press, New York

Gibson MM (1963) Spectra of turbulence in a round jet. J Fluid Mech 15: 161–173

Law AW-K; Wang H (1998) Simultaneous velocity and concentration measurements of buoyant jet discharges with combined DPIV and PLIF. 2nd Int Symp on Environmental Hydraulics, Hong Kong, pp 211–216, Publisher: Balkema: Rotterdam, Netherlands

Lemoine F; Wolff M; Lebouche M (1996) Simultaneous concentration and velocity measurements using combined laser-induced fluorescence and laser Doppler velocimetry: application to turbulent transport. Exp Fluids 20: 319–327

Papanicolaou PN; List EJ (1988) Investigation of round vertical turbulent buoyant jets. J Fluid Mech 195: 341–391

Tennekes H; Lumley JL (1972) A first course in turbulence. The MIT press, Cambridge, MA

Wygnanski I; Fiedler H (1969) Some measurements in the self-preserving jet. J Fluid Mech 38: 577–612